

A Wave Optics Propagation Code for Multi-Conjugate Adaptive Optics (Draft 04/22/01)

B.L. Ellerbroek¹

Gemini Observatory
670 N. A'ohoku Place
Hilo, Hawaii 96720

ABSTRACT

We describe the purpose, theory, implementation, and sample results of a wave optics propagation simulation developed to study multi-conjugate adaptive optics for 4-10 m class telescopes. This code was developed to assess the impact of diffraction effects and a variety of implementation error sources upon the performance of the Gemini-South MCAO system. These effects include: Hartmann sensing with extended and elongated laser guide stars, optical propagation effects through the optics and atmosphere, laser guide star projection through the atmosphere, deformable mirror and wave front sensor misregistration, and calibration for non-common path errors. The code may be run in either a wave optics or geometric propagation mode to allow the code to be anchored against linear analytical models and to explicitly evaluate the impact of diffraction effects. The code is written in MATLAB, and complete simulations of the Gemini-South MCAO design (including 3 deformable mirrors with 769 actuators, 5 LGS WFS with 1020 subapertures, 3 tip/tilt NGS WFS, and 50 meter phase screens with 1/32nd meter resolution) are possible using a Pentium III but require 1 to 6 days. Sample results are presented for Gemini-South MCAO as well as simpler AO systems. Several possibilities for parallelizing the code for faster execution and the modeling of ELTs are discussed.

Keywords: Multi-conjugate adaptive optics, adaptive optics modeling, extremely large telescopes

1 INTRODUCTION

The subject of performance evaluation for multi-conjugate adaptive optics (MCAO) [1] has already received considerable attention. Numerous studies of predicted performance are now available, many of them using analytical methods [2, 3, 4, 5] that are generalizations of techniques previously used to evaluate simpler adaptive optics (AO) systems [6, 7, 8]. Monte Carlo simulations have also been used to estimate MCAO performance [9]. All of these methods have obtained broadly consistent results. This is not too surprising, since they are all based upon a common first-order model for the AO system and the turbulence-induced phase errors to be corrected. Some of the basic elements of this model include: Optical phase distortions obtained by geometric ray tracing through the atmosphere and optical system, wave front sensor measurements that are linear functions of these phase profiles summed with additive noise, and a perfectly aligned and calibrated AO system. These assumptions simplify the computation of optimal reconstruction algorithms and best-case performance estimates for an ideal MCAO system, but higher-fidelity models will be required to address a range of more involved issues as the design work on real MCAO systems progresses. Some of these issues include:

- The nonlinearities and dynamic range limitations of Shack Hartmann (SH) sensors and other wave front sensing approaches;

¹Further author information –
Email: bellerbroek@gemini.edu; Telephone: (808) 974-2575; Fax: (808) 935-9235

- Scintillation and diffraction effects in the optics and atmosphere;
- Laser guide star (LGS) elongation, aberrations, and pointing errors;
- Deformable mirror (DM) and wave front sensor (WFS) misregistration errors;
- Non-common path wave front errors;
- WFS gain and bias calibration in the presence of the above; and
- AO control loop temporal dynamics.

We are now developing a Monte Carlo wave optics propagation simulation to investigate these higher-order effects. This paper provides a brief description of this simulation and presents sample results generated to date for the planned Gemini-South MCAO configuration.

Recent advances in microprocessor performance have greatly reduced the drudgery involved in developing and applying a propagation simulation to model a very-high-order AO system on a large telescope. Some of the improvement in processor speed can be given back to allow the use of higher-level languages, such as MATLAB or IDL, that provide a much more efficient and flexible development environment at the expense of some reduction in efficiency. Very large simulation cases are still tractable using this approach. The Gemini-South MCAO simulation, for example, includes 3 DM's with a total of 769 actuators, 3 natural guide star (NGS) and 5 LGS WFS's with a total of 1026 subapertures, and 7 atmospheric phase screens with an extent of 52.5 meters and a spatial resolution of 3.125 or 6.25 centimeters. These cases can be run on a 1 GHz Pentium III with 768 Mbytes of RAM, although the ratio between computer time and simulated time is in the range from 10^5 to 5×10^6 , depending upon the range of simulation features included from the above list. This is still efficient enough to enable simulation runs to be completed in from a few hours to less than a week. These simulation results can be used to help quantify the impact of many MCAO system design parameters (e.g. the allowable DM-to-WFS misregistration) and increase confidence in MCAO performance predictions before the system is actually built. The significant costs and predicted high payoffs associated with implementing MCAO on 8 to 10 meter class telescopes make detailed and accurate modeling particularly important. This will be even more true for extremely large telescopes (ELT's), where wave optics propagation simulations of MCAO should still be possible using parallel processing.

The remainder of the paper is organized as follows. Section 2 is a qualitative overview of the features included in the simulation code. Section 3 is a brief summary of the steps in each simulation run, and Section 4 describes some of the basic mathematical models used for simulation operations such as optical propagation and Shack-Hartmann wave front sensing. Section 5 summarizes sample simulation results for conventional AO systems, computed without wave optics propagation effects, and compares them against analytical predictions in an exercise to validate the code. Section 6 contains a few illustrative results on the effects of wave optics propagation and DM-to-WFS misregistration for a conventional AO system. Section 7 then presents a range of results for the Gemini-South MCAO design, and Section 8 concludes with a few comments on how this work might extended to consider ELT's.

2 SIMULATION OVERVIEW

Figure 1 is a schematic/cartoon illustrating the principal features included in the simulation. Atmospheric turbulence is modelled by one or more discrete, translating, periodic phase screens with approximately Kolmogorov or von Karman statistics. Optical propagation through the atmosphere can be modelled via either geometric ray tracing or wave optics, the latter implemented via a standard nearfield FFT propagator. Guide star constellations may be defined to include one or several NGS and one or several LGS at a common range. All guide stars within each of these classes currently share common magnitude and WFS characteristics. Laser guide stars may be modelled as either point or extended sources, with the shape of the latter depending upon the initial laser beam profile, the aberrations

induced by the uplink propagation, and the vertical distribution of the backscatter layer. AO system performance is evaluated in terms of the mean point spread function and Strehl ratio time history at one or several points in the field-of-view.

The telescope and AO system are modelled as one or more additional phase screens beginning with the telescope primary mirror. Each surface is defined in terms of a conjugate range, an amplitude transmittance profile, and a phase profile. The phase profile may include static figure errors and the dynamic adjustments applied to deformable and tip-tilt mirrors. Optical propagation from surface to surface is implemented using the same propagator as used for the atmosphere. The propagation path for each WFS and evaluation field point may also include a non-common path phase screen conjugate to the telescope entrance pupil.

The phase correctors currently modelled include two-axis tip/tilt mirrors and “zonal” deformable mirrors with a square actuator pattern. This pattern may be misaligned in five degrees of freedom (x - and y translation, rotation, and x - and y magnification) with respect to the ideal. Wave front sensors are currently limited to SH sensors with square actuator geometries. This geometry may be arbitrarily distorted with respect to an ideal square pattern to simulate pupil distortion. Each SH lenslet array is located conjugate to the pupil of the telescope. WFS measurements may be modelled either geometrically as the average wavefront gradients over each subaperture, or as centroids computed from the guide star images as recorded by cells of n by n pixels behind each lenslet in the SH array. Photon and detector read noise may be included in the pixel values. Laser guide star images are modelled isoplanatically by convolving the guide star intensity distribution in the sodium layer with a subaperture PSF computed for a point source at the average layer range. The raw centroids are gain- and bias calibrated to account for non-common path phase errors, the nominal atmospheric seeing, and the nominal intensity distribution of the LGS.

The actuator commands to each DM and tip/tilt mirror (TTM) are computed using a minimal variance reconstruction algorithm as previously described [3]. The reconstructed actuator estimates are filtered by discrete finite difference equations before they are applied to the active mirrors, with two separate sets of coefficients specifiable for the DM’s and the TTM. Actuator temporal dynamics are modelled as a damped harmonic oscillator. The fast tip/tilt mirror may be offloaded to a second slow tip/tilt mirror (such as the telescope secondary mirror). LGS pointing mirrors may also be driven to null the average tilt measurement from each LGS WFS. The overall control system architecture is quite standard, but other approaches, such as modal or predictive control, could be simulated with relatively modest modifications to the code.

Some of the features presently not modelled include (i) windshake and other dynamic errors in the optical system, (ii) DM actuator hysteresis and finite dynamic range, (iii) advanced or nonstandard control algorithms, and (iv) background noise from either the sky or Rayleigh backscatter.

3 SIMULATION SEQUENCE

This section gives a brief summary of the sequence of processing steps that comprise a single simulation run.

3.1 Parameter definition

The user-input parameters that specify the scenario to be simulated are divided into seven categories: General parameters (simulation length, phase screen size and resolution, etc.), atmospheric model, performance evaluation directions and wavelengths, telescope optical surfaces, WFS parameters, DM and TTM parameters, and control algorithm parameters. These values are defined, stored, and modified using a simple menu-driven interface.

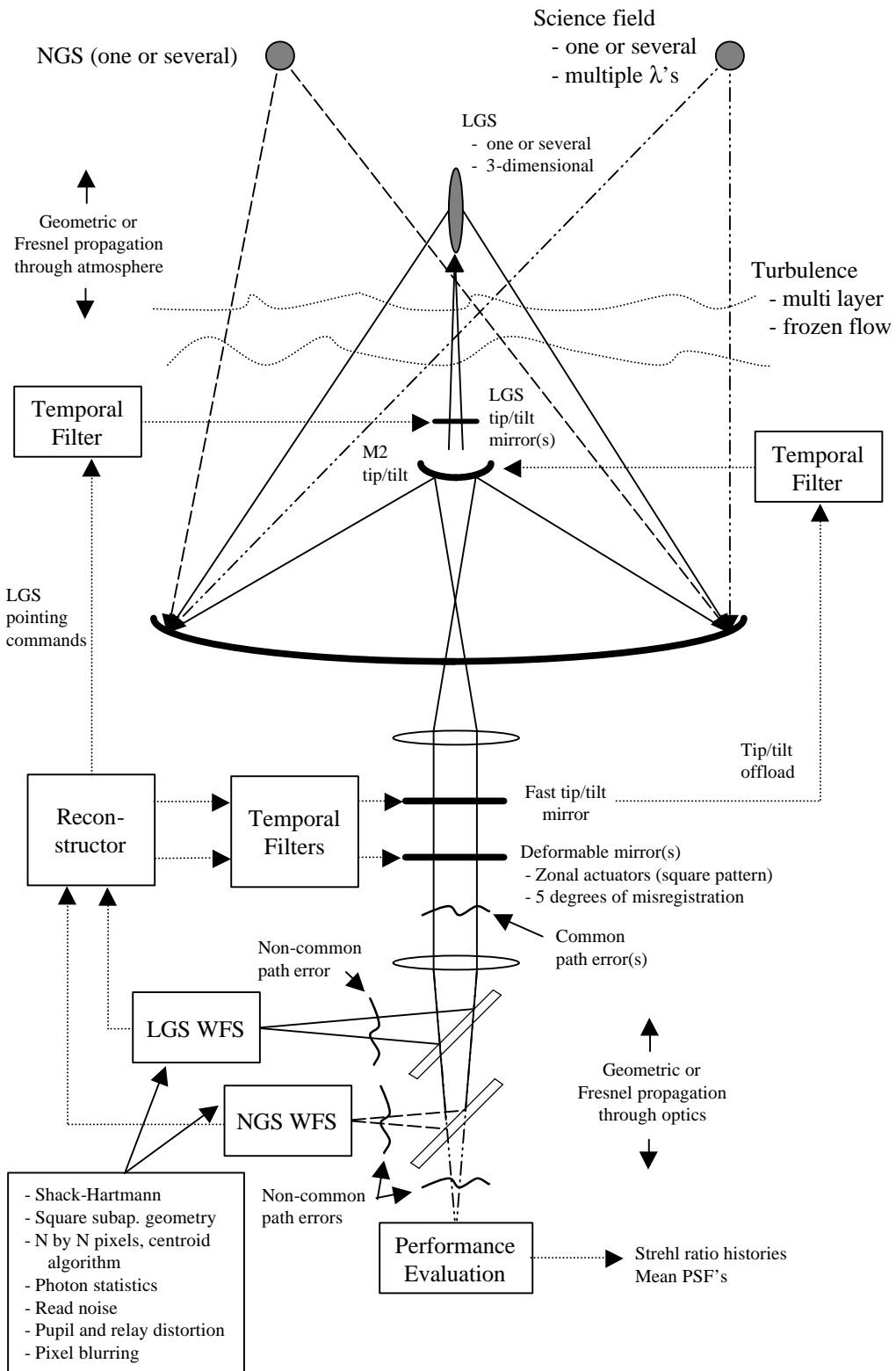


Figure 1: Simulation Features

This schematic/cartoon illustrates the basic features of the wave optics propagation simulation.

3.2 Scenario Generation

This step builds most of the data structures describing the AO system and the atmosphere, including the following quantities:

- The telescope clear aperture function.
- Amplitude and phase profiles for the remaining optical surfaces in the telescope and the LGS lasers. These functions are input from files that have been precomputed by the user.
- DM actuator locations and influence functions.
- DM commands to minimize the residual static aberrations in the science path. These commands are computed to minimize the mean-square wavefront error over the set of evaluation directions, assuming perfect knowledge of the non common path errors.
- WFS subaperture locations and geometric “influence functions.”
- WFS biases and gains.
- The Geometric DM-to-WFS influence matrix. This will be used to compute the reconstruction algorithm.
- The simulation event list (see section 3.4 below).
- Atmospheric phase screens.
- The initial (zeroed) state of the AO control loops.

The simulation starting conditions are saved to a file to simplify setting up multiple runs with slight variations to the parameters (e.g., selecting geometric or wave-optics propagation with all other parameters held constant).

3.3 Reconstructor Computation

The wavefront reconstruction matrix is computed to minimize the field- and aperture averaged mean-square residual wavefront error over the set of evaluation directions specified by the user in subsection 3.1 above. The simulation generates an input file for an existing FORTRAN program that computes the reconstruction matrix and estimates AO performance assuming geometric propagation and no misregistration or non common path errors. For simulations including a separate tip/tilt mirror, the reconstruction matrix is decomposed into separate components for the DM’s and the TTM.

3.4 Time Domain Simulation

The Monte Carlo simulation proper is driven by an event list that describes the order of execution of a set of high-level operations that are the building blocks of the simulation time line. Each element of the list comprises an event type, the time for the initial occurrence of the event, the repetition interval, and one or several event-specific parameters. The simulation driver repeatedly scans through this list, locates and executes the next event to occur, and increments the time of that event by its repetition interval. This approach allows a wide range of timelines to be simulated by simple adjustments to the scenario input parameters. The currently implemented set of events includes:

- Evaluate performance: Loop over the evaluation directions and wavelengths. For each direction and wavelength, propagate a plane wavefront from infinity through each atmospheric phase screen and optical surface, with each phase profile computed at the current time using either the Taylor hypothesis (for phase screens) or the damped harmonic oscillator model (for DM's and the TTM). Propagate to the far field, record the Strehl ratio, and accumulate the mean PSF.
- Accumulate signal for WFS class i : The class i is either 1 or 2 for the NGS or LGS WFS measurements. Loop over the guide star directions and (for polychromatic NGS) wavelengths. For each direction and wavelength, propagate a plane wavefront from the guide star through each atmospheric phase screen and optical surface, with each phase profile computed at the current time. Compute the instantaneous WFS measurement, either in terms of subaperture-averaged wavefront gradients or the subaperture PSFs on the Shack-Hartmann array. For laser guidestars, propagate the laser beam up through the atmosphere (at the appropriate earlier point in time), and convolve each subaperture PSF with the LGS intensity distribution in the sodium layer. Add the instantaneous WFS signal (either mean wavefront gradient or pixel intensities) to the accumulated signal for the current integration time. (Accumulating multiple WFS measurements during each integration time improves the modeling of control loop temporal dynamics, but this feature has not been exercised for any of the results presented in this report).
- Readout WFS class i : For geometric simulations, add measurement noise to each accumulated gradient measurement and zero the accumulated measurements for the next integration time. For wave optics simulations, add photon and detector noise to each pixel, compute SH spot centroids from the noisy pixel values, and zero the accumulated measurements for the next integration time. Apply gain and bias calibration to the measurements in either case (although the gain calibration is always unity for geometric simulations).
- Update DM actuator commands: Compute the current values of the DM actuator positions from their positions at the previous cycle, the commands applied at the beginning of the previous cycle, and the damped harmonic oscillator model. Multiply the most current set of WFS measurements by the DM reconstruction matrix, and filter the estimated actuator errors by the DM finite difference equation to determine the new set of actuator commands. The new actuator commands and positions will be used to compute the figures of the deformable mirrors for any optical propagations that occur between this time and the next DM command update.
- Update fast TTM commands: This is similar to updating the DM actuator commands, except that the TTM parameters are used for the values of the reconstruction matrix, the finite difference equation, and the damped harmonic oscillator model.
- Offload the fast TTM to the slow TTM: Compute the current positions of the slow TTM actuators as above. Compute the new commands to the slow TTM actuators, using the current commands to the fast TTM as the error signals to the slow TTM finite difference equation.
- Update the LGS pointing mirror commands: Compute the current positions of the LGS pointing mirror actuators as above. Compute the new commands to the pointing mirrors, using the average tilt measurement from each LGS WFS as the error signal to the pointing mirror finite difference equation.
- Stop: Exit the simulation loop.

3.5 Postprocessing

At present, this step simply averages the accumulated PSF's to determine the mean PSF for each evaluation direction and wavelength, and then outputs these mean PSF's and the Strehl ratio time histories to a file for later analysis. It is relatively straightforward to augment these two quantities with additional data (e.g., the DM actuator commands at each simulation cycle) on a case-by-case basis for either debugging purposes or a more detailed analysis of AO loop performance.

4 SIMULATION MODELS

This section describes in somewhat greater detail the basic mathematical models used for some of more fundamental quantities used and operations performed by the simulation. Readers should be careful not to assume continuity of notation across subsection boundaries.

4.1 Phase Screen Generation

The simulation computes atmospheric phase screen realizations as spatially filtered white noise according to the formula

$$\text{OPD}(\vec{x}) = c \Re \left\{ \mathcal{F} \left[\sqrt{\Phi(\vec{\kappa})} (r(\vec{\kappa}) + ir'(\vec{\kappa})) \right] \right\}, \quad (1)$$

where OPD is the phase screen, \mathcal{F} is the 2-dimensional spatial Fourier transform, Φ is the spatial power spectrum of the turbulence, $\vec{\kappa}$ is a spatial frequency variable, r and r' are zero mean, unit variance, real-valued white noise functions, and c is a scaling factor for the strength of the screen. For a von Karman turbulence spectrum, the function Φ takes the form

$$\Phi(\vec{\kappa}) = |\kappa^2 + (W/L_0)^2|^{-11/6}, \quad (2)$$

where W is the width of the phase screen and L_0 is the turbulence outer scale. Setting $L_0 = \infty$ yields the usual Kolmogorov spectrum. Finally, the constant c is defined by the expression

$$c = 0.1517 \sqrt{f} \left(\frac{W}{r_0} \right)^{5/6} \left(\frac{\lambda}{2\pi} \right), \quad (3)$$

where f is the fraction of the integrated atmospheric turbulence strength in the layer, and r_0 is the turbulence-induced coherence diameter at wavelength λ . This definition for the scaling factor c yields a phase screen expressed as an optical path difference, not as radians of phase at a particular wavelength.

Eq. (1) is implemented via a fast Fourier transform (FFT), and the resulting phase screens are periodic. The width W of the phase screen must therefore be considerably larger than the telescope aperture diameter, and it should ideally also be large compared to the turbulence outer scale. The amount of turbulence in low-order modes will be underestimated if this second condition is not satisfied. Sample results in Section 5 below illustrate that performance estimates for closed loop AO are generally not a very strong function of the outer scale or the width of the phase screens, however.

4.2 Optical Propagation

Wave optics propagation from plane to plane is modelled as a spatial filtering operation, namely

$$U_{n+1}(\vec{x}) = \mathcal{F} \left[\exp(i\pi\kappa^2\lambda z) \mathcal{F}^{-1} (U_n(\vec{y}) S_n(\vec{y})) \right] (\vec{x}). \quad (4)$$

Here U_n is the optical field immediately before encountering the (multiplicative) phase screen S_n at layer number n , \mathcal{F} is still the two-dimensional spatial Fourier transform operator, λ is the wavelength, and z is the distance from layer n to layer $n + 1$. The complex field U_n is related to the amplitude a and phase ϕ of the beam by the equation

$$U_n(\vec{x}) = a_n(\vec{x}) \exp(i\phi_n(\vec{x})), \quad (5)$$

and the complex phase screen S_n is similarly related to the optical path difference OPD_n and amplitude transmittance function t_n :

$$S_n(\vec{x}) = t_n(\vec{x}) \exp(2\pi i \text{OPD}_n(\vec{x})/\lambda) \quad (6)$$

The transmittance function t_n is used to define the telescope clear aperture, and possibly other aperture and/or field stops within the optical system.

Eq. (4) may be used for both upwards and downwards propagation though both the atmosphere and optics. The initial field U_0 is a infinite flat or spherical wavefront at the top of the atmosphere for downwards propagation, and is equal to the laser beam profile at the launch telescope for LGS propagation up through the atmosphere. The propagation distance z is treated as positive in both cases, except in the event that an optical relay forms an image of a plane located earlier along the propagation path. This occurs in an MCAO system, for example, when a wavefront propagates from the telescope aperture to a deformable mirror optically conjugate to a nonzero altitude.

Eq. (4) cannot be implemented exactly as written using FFT's, since the input field U_0 will oscillate extremely rapidly for a guide star that is off-axis or at finite range due to the resulting linear (tilt) and quadratic (focus) terms present in the phase function ϕ_0 . The case of an off-axis star may be treated by defining a new coordinate system with the z axis parallel to the direction of propagation. Making a paraxial approximation, the propagation equation now becomes

$$U_{n+1}(\vec{x} + z_{n+1}\vec{\theta}) = \mathcal{F} \left[\exp(i\pi\kappa^2\lambda z) \mathcal{F}^{-1} \left(U_n(\vec{y} + z_n\vec{\theta}) S_n(\vec{y} + z_n\vec{\theta}) \right) \right] (\vec{x}), \quad (7)$$

where $\vec{\theta}$ is the direction of the source, and z_n and z_{n+1} are the z coordinates of the two layers. Eq. (7) may also be obtained by explicitly identifying the nominal tilt term $2\pi\vec{\theta} \cdot \vec{x}/\lambda$ in the wavefront ϕ_n and applying the Fourier shift theorem. For numerical calculations, the values of the phase screen S_n will need to be interpolated except in the very special case that the offset $z_n\vec{\theta}$ is exactly divisible by the simulation grid spacing. Our subjective experience is that this interpolation is best performed via the Fourier shift theorem,

$$S_n(\vec{x} + z_n\vec{\theta}) = \mathcal{F} \left[\exp(-2\pi i z_n \vec{\theta} \cdot \vec{\kappa}) \mathcal{F}(S_n(\vec{y})) \right] (\vec{x}), \quad (8)$$

since linear and even cubic spline interpolation will amplify the high spatial frequency content of the screen. The same technique can be used to translate phase screens with time according to the Taylor (frozen flow) hypothesis, and in fact the net effect of these two operations can be implemented in a single step.

For a guide star located at a finite range z_f , the propagation equation is further modified to take the form

$$U_{n+1} \left[\left(\frac{z_f - z_{n+1}}{z_f - z_n} \right) \vec{x} + z_{n+1}\vec{\theta} \right] = \mathcal{F} \left\{ \exp \left[i\pi\kappa^2\lambda z \left(\frac{z_f - z_n}{z_f - z_{n+1}} \right) \right] \mathcal{F}^{-1} \left(U_n(\vec{y} + z_n\vec{\theta}) S_n(\vec{y} + z_n\vec{\theta}) \right) \right\} (\vec{x}), \quad (9)$$

where the nominal spherical term of the wavefront ϕ_n is also dropped in this expression. One way to derive this expression is to propagate both $S_n U_n$ and U_{n+1} to the plane $z = z_f$ with no intervening phase aberrations using the usual far field propagator [11], and set the two results equal. Solving this relationship for U_{n+1} yields Eq. (9).

Because of the scale factor appearing before \vec{x} on the left hand side of Eq. (9), the fields U_n and U_{n+1} will be evaluated on two different meshes when the propagation equation is implemented using FFT's. The mesh spacing for each screen is proportional to the distance from the screen to the focal plane at $z = z_f$, so Eq. (9) is sometimes described as using a converging coordinate system. This is significant for simulation purposes because the atmospheric screens S_n must now be evaluated on two different meshes for the LGS and NGS propagations. It is much more computationally efficient to interpolate each screen only once and save the results if sufficient memory is available.

4.3 Active Mirrors

Deformable- and tip-tilt mirror phase adjustments are modeled using the usual linear superposition approximation,

$$\text{OPD}(\vec{x}) = \sum_i p_i h_i(\vec{x}), \quad (10)$$

where p_i is the position (displacement) of actuator number i , and $h_i(\vec{x})$ is the influence function for that actuator. Hysteresis and saturation are not considered at this time. For deformable mirrors, the influence function h_i is a simple two-dimensional linear spline, with the actuators nominally located on a square grid. The actuator locations may be misaligned in x - and y displacement, rotation, and x - and y magnification. The influence functions will be similarly distorted in this case.

The position of each actuator is determined according to the differential equation

$$c(t) = kp(t) + dp'(t) + mp''(t), \quad (11)$$

where $c(t)$ is the (position) command to the actuator, and the coefficients k , d , and m describe the dynamics of a damped harmonic oscillator. This model is used for the deformable mirrors, the fast tip/tilt mirror, the slow tip/tilt mirror, and the LGS pointing mirrors, although different coefficients may be defined for each mirror class. One method for solving Eq. (11) is to transform it into the form

$$\vec{x}'(t) = A\vec{x}(t) + B(t), \quad (12)$$

which may be solved using Laplace transforms with the result

$$\begin{aligned} \vec{x}(t) &= e^{At}\vec{x}(0) + A^{-1}(e^{At} - I)B \\ &= U [e^{\Lambda t}U^{-1}\vec{x}(0) + \Lambda^{-1}(e^{\Lambda t} - I)U^{-1}B], \end{aligned} \quad (13)$$

where

$$A = U\Lambda U^{-1}, \quad (14)$$

is the eigenvalue-eigenvector decomposition of the matrix A . If $m = 0$, then the required variable transformation is just $x(t) = p(t)$, $A = -k/d$, and $B = c/d$. If m is nonzero, these definitions become

$$\vec{x}(t) = \begin{pmatrix} p(t) \\ p'(t) \end{pmatrix} \quad (15)$$

$$A = \begin{pmatrix} 0 & 1 \\ -k/m & -d/m \end{pmatrix} \quad (16)$$

$$B = \begin{pmatrix} 0 \\ c/m \end{pmatrix} \quad (17)$$

4.4 Image Formation

The simulation uses the usual propagation equation to compute the far-field point spread function (PSF) associated with an optical field U ,

$$\text{PSF}(\vec{\theta}) = |\mathcal{F}(U(\vec{x}))|^2 (\vec{\theta}/\lambda). \quad (18)$$

This same equation is used to compute Shack-Hartmann spots and laser guide star intensity distributions as described further below.

4.5 Wavefront Sensing

For geometric simulations, we use the usual first order approximation for the wavefront gradient (or slope) measurement \vec{s} obtained from a Shack-Hartmann sensor:

$$\vec{s} = \left[\int d\vec{x} W_{sa}(\vec{x}) \right]^{-1} \int d\vec{x} W_{sa}(\vec{x}) \nabla \text{OPD}(\vec{x}) + \vec{n} \quad (19)$$

Here W_{sa} defines the areas of the subaperture, ∇ is the gradient operator, OPD is the input wave front expressed as an optical path difference, and \vec{n} is additive white noise.

For wave optics simulations, each subaperture tip/tilt measurement from the SH WFS is modeled as a centroid computed from noisy measurements of the subaperture Shack-Hartmann spot. The formula for the gradient \vec{s} on a single subaperture becomes

$$\vec{s} = g^{-1} \left[\left(\sum_i c_i \vec{p}_i / \sum_i c_i \right) - \vec{b} \right], \quad (20)$$

where g and \vec{b} are gain and bias calibration factors computed as described below, c_i is the number of photodetection events (or counts) on pixel number i in the subaperture, and \vec{p}_i are the focal plane coordinates of pixel number i (Quadrant detectors have been used in all simulations to date). The pixel output c_i is modeled as the sum of a Poisson process plus zero mean, normally distributed detector read noise. For a given input field incident upon the SH array, the mean value of c_i is described by the expression

$$\begin{aligned} \bar{c}_i &= \int d\vec{x} \bar{I}(\vec{x}) W_p(\vec{x} - \vec{p}_i) \\ &= \int d\vec{\kappa} \mathcal{F}(\bar{I})(\vec{\kappa}) [\mathcal{F}(W_p)(\vec{\kappa})]^* \exp(2\pi i \vec{p}_i \cdot \vec{\kappa}), \end{aligned} \quad (21)$$

where \bar{I} is the probability density function for the Shack-Hartmann spot, W_p is the nominal responsivity function for a single detector, \vec{p}_i is again the location of pixel number i , and the superscript “*” denotes complex conjugation. The second equality follows from the Plancherel theorem and the Fourier shift theorem, and is the formula actually implemented in the simulation.

For NGS wavefront sensing, the Shack-Hartmann spot is evaluated using the formula

$$\bar{I}(\vec{\theta}) \propto \text{PSF}_{sa}(\vec{\theta}), \quad (22)$$

where the point spread function PSF_{sa} is computed from Eq. (18) with the optical field U multiplied by the subaperture transmittance function W_{sa} . For LGS wavefront sensing, this PSF must be convolved with the three-dimensional intensity profile of the LGS in the sodium layer:

$$\bar{I}(\vec{\theta}) \propto \text{PSF}_{sa}(\vec{\theta}) * \text{PSF}_{lb}(\vec{\theta}) * e(\vec{\theta}), \quad (23)$$

where PSF_{lb} is computed according to Eq. (18) with U equal to the laser beam intensity profile at the top of the atmosphere, and e is an elongation factor that is a function of the separation between the launch telescope and the subaperture. This one-dimensional elongation factor is given to first order by the expression

$$e(\vec{\theta}) \propto \delta(\vec{\theta} \cdot \vec{r}_\perp) d[\bar{z}(1 - \bar{z}\theta/r^{-1})]. \quad (24)$$

Here δ is the usual Dirac delta function, \vec{r} is the separation between the launch telescope and the subaperture, \vec{r}_\perp is a unit vector orthogonal to \vec{r} , $d(z)$ is the density of the sodium layer as a function of altitude, and \bar{z} is the mean range to the sodium layer.

By using Eq. (23), we are implicitly assuming that (i) the shape of the two-dimensional LGS cross section is constant through the sodium layer, (ii) the extent of the guide star is small compared to the isoplanatic patch size for a subaperture, and (iii) the LGS WFS is correctly focussed and boresighted with respect to the LGS. The constants of proportionality in Eq.’s (22) and (23) are set to yield the desired mean signal level for each SH subaperture. Transforming to the Fourier domain, Eq. (23) becomes

$$\mathcal{F}(\bar{I})(\vec{\kappa}) \propto \mathcal{F}(\text{PSF}_{sa})(\vec{\kappa}) \mathcal{F}(\text{PSF}_{lb})(\vec{\kappa}) \mathcal{F}(e)(\vec{\kappa}). \quad (25)$$

This expression for $\mathcal{F}(\bar{I})$ is used in Eq. (21) to compute mean signal levels for each WFS pixel.

It remains to describe the calculation of the gain and bias calibration coefficients g and \vec{b} . The bias \vec{b} is equal to the centroid computed for a long-exposure SH spot that has been ensemble averaged over atmospheric turbulence statistics, and the gain g is computed by “scanning” this average spot across the SH detector array. Neglecting outer scale effects, the Fourier transform of an ensemble-averaged NGS SH spot is given by the expression

$$\langle \mathcal{F}(\bar{I}(\vec{\kappa})) \rangle \propto \mathcal{F}(\text{PSF}_{sa,0})(\vec{\kappa}) \exp[-3.44(\lambda\kappa/r_0)^{5/3}], \quad (26)$$

where the angle brackets, $\langle \dots \rangle$, denote averaging over turbulence statistics, r_0 is again the turbulence induced effective coherence diameter, and $\text{PSF}_{sa,0}$ is the Shack-Hartmann spot computed for the wave front distortions present in the optical system without atmospheric turbulence effects. For LGS SH spots, the corresponding formula is

$$\langle \mathcal{F}(\bar{I}(\vec{\kappa})) \rangle \propto \mathcal{F}(\text{PSF}_{sa,0})(\vec{\kappa}) \mathcal{F}(\text{PSF}_{lb,0})(\vec{\kappa}) \mathcal{F}(e)(\vec{\kappa}) \exp[-6.88(\lambda\kappa/r_0)^{5/3}], \quad (27)$$

where $\text{PSF}_{lb,0}$ is the far field intensity profile for the laser beam with no additional turbulence-induced phase errors. This last expression includes a factor of 6.88, not 3.44, in the long-exposure filter function because turbulence degrades both the LGS intensity distribution in the sodium layer and the WFS subaperture PSF. Any correlations between the effects of aberrations on the uplink and downlink are neglected in the calculation of g and \vec{b} , but not in the simulation itself.

4.6 Wavefront Reconstruction and Loop Filtering

For simulations without a separate tip/tilt mirror, the current error \vec{e} in the DM actuator command vector is estimated using the equation

$$\vec{e} = E\vec{s}, \quad (28)$$

where E is the reconstruction matrix and \vec{s} is combined WFS measurement vector. Full aperture wavefront tilt is projected off each individual LGS WFS measurement vector before the combined vector \vec{s} is assembled. The reconstruction matrix E is computed by a separate analysis program using methods described previously [3]. It is derived assuming geometric optics and a Kolmogorov turbulence spectrum, using the DM-to-WFS influence matrix computed by the simulation code.

For simulations that do include a separate tip/tilt mirror, the DM and TTM actuator errors are computed in parallel using two separate reconstruction matrices by the formulas.

$$\vec{e}_{dm} = P_{dm}E\vec{s} \quad (29)$$

$$\vec{e}_{ttm} = P_{ttm}E\vec{s} \quad (30)$$

The matrix P_{dm} simply removes the overall tip/tilt component from a DM actuator command vector, and P_{ttm} converts this tip/tilt component (or the sum of the components from multiple DM’s) into corresponding tip/tilt mirror actuator commands.

The actuator error vectors are temporally filtered by finite difference equations to compute the commands applied to the deformable and tip/tilt mirrors. These filters are of the form

$$\vec{c}(n) = \sum_{i=1}^n a_i \vec{c}(n-i) + \sum_{i=0}^{n-1} b_{i+1} \vec{e}(n-i), \quad (31)$$

where $\vec{e}(n)$ is the error vector at cycle n , and $\vec{c}(n)$ is the resulting command vector. Signal processing latency can be simulated by shifting the coefficients b_i to a later time. Two separate sets of coefficients a_i and b_i may be specified for the tip/tilt and deformable mirrors. Similar equations are used to drive the slow tip/tilt mirror and the LGS pointing mirrors, except that the definitions for the error vectors \vec{e} are somewhat different. For the slow tip/tilt mirror, the vector \vec{e} is the current command to the fast tip/tilt mirror. For the LGS pointing mirrors, the vector \vec{e} is comprised of the full aperture tip/tilt measurements on the LGS WFS.

5 SIMULATION VALIDATION

In this section, we report on a test suite of simulation results that were generated for a relatively simple AO system to verify the correctness of the MATLAB code. All of the simulation results were obtained using geometric propagation, so that exact agreement between analysis and simulation could in principal be achieved. Three set of simulation runs were performed to parameterize the impact of (i) servo lag, (ii) WFS measurement noise, and (iii) common anisoplanatism. The simulated AO system consisted of an 8-meter telescope with 6 by 6 DM actuators and 5 by 5 SH WFS subapertures. The simulations used a 256 by 256 point propagation grid with a mesh of 0.2 meters, yielding a phase screen width of 51.2 meters. The simulation runs parameterizing WFS noise and servo lag effects used a single atmospheric phase screen, while the anisoplanatism simulations used a 5-layer approximation to the median Cerro Pachon turbulence profile. In both cases the value of the turbulence induced effective coherence diameter, r_0 , was equal to 0.166 m at a wavelength of $0.5 \mu\text{m}$.

The simulations were scored by comparing the average Strehl ratios for 100 simulation cycles against analytical performance predictions. Exact agreement is too much to expect for several reasons. There is some randomness in the average results after only 100 iterations, there are slight numerical differences between simulated and analytical values of the DM-to-WFS influence matrices, and the power spectra of the turbulence-induced phase errors are also not identical. In particular, the simulation phase screens are periodic, and have an effective outer scale of no more than $51.2/2 = 25.6$ meters, even if the outer scale parameter L_0 is set to infinity. Simulation runs and analytical Strehl calculations were made for both $L_0 = \infty$ and $L_0 = 25.6$ m to study the impact of this approximation. The finite outer scale improved Strehls ratios by typically 1-3 per cent (absolute) for both analysis and simulation, with the simulation results for $L_0 = \infty$ matching the analytical predictions for $L_0 = 25.6$ m very closely in most cases. The overall level of agreement between the analysis and simulation Strehls was on the order of 1-2 per cent (absolute).

5.1 WFS noise

To isolate the effect of WFS measurement noise from servo lag and anisoplanatism, we defined a simulation timeline with performance evaluation occuring immediately after the DM actuator commands were updated, using an instantaneous WFS measurement and a control loop gain of unity. We considered two different nonzero levels of additive WFS measurement noise and three different evaluation wavelengths to obtain a range of Strehl ratios between 0.07 and 0.60. Table 1 summarizes the mean simulation results and the corresponding analytical calculations for outer scales of 25.6 meters and infinity.

5.2 Servo Lag

For this comparison, we zeroed the WFS measurement noise and instead varied the bandwidth of the AO control loop. We simulated a pure integrator control law, with a gain g of 1.0, 0.5, and 0.33. The results obtained are summarized in Table 2.

5.3 Common Anisoplanatism

In this case, we evaluated performance at offsets of 10 and 20 arc sec from the guidestar with a loop gain of unity and zero WFS measurement noise. The results are summarized in Table 3. Each of the off-axis results is actually an average over 8 evaluation directions distributed uniformly around a circle.

Wavelength, μm	σ_θ , arc sec	Analysis Strehl		Simulation Strehl	
		$L_0 = 25.6 \text{ m}$	$L_0 = \infty$	$L_0 = 25.6 \text{ m}$	$L_0 = \infty$
1.65	0.0	0.183	0.205	0.207	0.230
	0.3	0.123	0.141	0.146	0.158
	0.6	0.073	0.083	0.088	0.093
2.20	0.0	0.380	0.406	0.410	0.436
	0.3	0.298	0.325	0.333	0.350
	0.6	0.212	0.232	0.244	0.252
2.90	0.0	0.571	0.594	0.598	0.619
	0.3	0.495	0.521	0.529	0.544
	0.6	0.401	0.425	0.436	0.447

Table 1: AO performance vs. WFS measurement noise

The quantity σ_θ is the one-axis, one-sigma measurement noise for each WFS subaperture tilt measurement.

Wavelength, μm	Loop gain, g	Analysis Strehl		Simulation Strehl	
		$L_0 = 25.6 \text{ m}$	$L_0 = \infty$	$L_0 = 25.6 \text{ m}$	$L_0 = \infty$
1.65	1.00	0.183	0.205	0.207	0.230
	0.50	0.124	0.148	0.133	0.161
	0.33	0.076	0.097	0.077	0.104
2.20	1.00	0.380	0.406	0.410	0.436
	0.50	0.302	0.336	0.320	0.357
	0.33	0.221	0.261	0.232	0.278
2.90	1.00	0.571	0.594	0.598	0.619
	0.50	0.499	0.532	0.519	0.553
	0.33	0.414	0.458	0.429	0.479

Table 2: AO performance vs. AO loop Gain

The quantity g is the loop gain for a sampled data control law of the form $c(n+1) = ge(n+1) + c(n)$, where $c(n)$ is the DM actuator command vector at cycle n , and $e(n)$ is the reconstructed wavefront error.

Wavelength, μm	θ , arc sec	Analysis Strehl		Simulation Strehl	
		$L_0 = 25.6 \text{ m}$	$L_0 = \infty$	$L_0 = 25.6 \text{ m}$	$L_0 = \infty$
1.65	0	0.183	0.205	0.207	0.230
	10	0.060	0.076	0.068	0.083
	20	0.018	0.022	0.016	0.019
2.20	0	0.380	0.406	0.410	0.436
	10	0.184	0.221	0.205	0.234
	20	0.058	0.076	0.055	0.074
2.90	0	0.571	0.594	0.598	0.619
	10	0.371	0.414	0.394	0.428
	20	0.160	0.202	0.164	0.204

Table 3: AO performance vs. anisoplanatism

The quantity θ is the angular offset between the natural guide star and the evaluation direction.

6 DIFFRACTION AND MISREGISTRATION

In this section we present a few sample results on these higher-order effects for conventional AO systems, primarily for the sake of comparison with the corresponding MCAO results to be described in Section 7 below.

6.1 Selecting the Grid Mesh

From the simulation results in Section 5, it appears that a grid width of about 50 meters and a grid mesh of about 0.2 meters are adequate to obtain geometric simulation results with Strehl ratios accurate to about 1-3 per cent (absolute) for the aperture diameters, evaluation wavelengths, and atmospheric turbulence profiles of interest for AO systems at Gemini South. The grid mesh Δx must be reduced when diffraction effects are simulated for two reasons. First, each WFS subaperture spot image at wavelength λ is computed on a grid of width $\lambda/\Delta x$, and this angle must be somewhat larger than both the diameter of the guide star and the width of the quadcell to avoid aliasing effects. For the Gemini-South MCAO design, the most stressing case is given by the LGS WFS with $\lambda = 0.589 \mu\text{m}$, a 2 arc sec quad cell width, and a guide star full width, half maxima of approximately 2 arc sec with elongation effects included. The grid mesh Δx must consequently be at least somewhat smaller than 1/16th of a meter.

Accurate modelling of scintillation and diffraction effects in the atmosphere also requires a fairly small value for Δx . One standard measure for scintillation is σ_χ^2 , the log-amplitude-variance of the aberrated field received at the ground from a uniform plane wavefront at the top of the atmosphere. Because the Cerro Pachon turbulence profile is relatively benign, this quantity is accurately described by the Rytov approximation

$$\sigma_\chi^2 = \frac{1.33k^{-5/6}r_0^{-5/3} \int dz C_n^2(z)z^{5/6}}{\int dz C_n^2(z)}, \quad (32)$$

where $k = 2\pi/\lambda$ is the wavenumber for the wavelength of propagation λ . Table 4 lists values of σ_χ^2 computed using Eq. (32) for the Cerro Pachon turbulence profile, and also the values obtained from simulation using grid meshes of 1/16 and 1/32 meters. Scintillation increases with decreasing λ , and according to Rytov theory $\sigma_\chi^2 = 0.0140$ at $\lambda = 0.589 \mu\text{m}$. The values of σ_χ^2 obtained by simulation at this wavelength are 0.0078 and 0.0121 for grid meshes of 1/16 and 1/32 meters, respectively. A mesh of 1/32 meters corresponds to a grid size of 1600 by 1600 points for a grid width of 50 meters, and this value provides an satisfactory level of simulation accuracy with feasible memory

Wavelength, μm	σ_χ^2 , Rytov Theory	σ_χ^2 , Simulation	
		Mesh = 1/16 meters	Mesh = 1/32 meters
0.589	0.0140	0.0078	0.0121
0.850	0.0091	0.0060	0.0083
1.250	0.0058	0.0043	0.0054
1.650	0.0042	0.0034	0.0040
2.200	0.0030	0.0025	0.0029

Table 4: Simulated Scintillation Results vs Rytov Theory

The quantity σ_χ^2 is the log-amplitude-variance for the scintillated wavefront received at the ground after propagation through a 7-layer approximation to the median Cerro Pachon turbulence profile.

and CPU requirements. The memory required for 7 double precision, complex-valued 1600^2 phase screens is about 287 Mbytes, which approximately doubles to about 600 Mbytes when a second set of screens is interpolated onto a converging coordinate system for the LGS propagations. The execution time for a single 1600^2 FFT is about xxx seconds in MATLAB for a 1 GHz Pentium III processor.

6.2 Diffraction

Figure 2 plots Strehl ratio time histories in K band for a conventional LGS AO system using parameters taken from the Gemini-South MCAO design as listed in Table 6 in Section 7 below. These results are for the case of an on-axis LGS and an on-axis tip/tilt NGS. The solid curve plots the results of a geometric simulation. The open-loop K band Strehl ratio of about 0.02 improves to somewhat over 0.8 in approximately 6 simulation cycles when the AO loop is closed. The mean Strehl ratio for cycles 11–100 is 0.815, compared with a analytical performance estimate of 0.799, with the slight discrepancy probably attributable to the effective finite outer scale imposed in the simulation by the periodic phase screens. The dashed curve plots the results of a wave optics simulation using the same atmospheric phase screen and an ideal point source LGS. The mean Strehl ratio after the warmup interval has been reduced slightly from 0.815 to 0.790 due to so-called “speckle noise” and other nonlinearities in the LGS and NGS WFS. Finally, the dot-dashed curve plots results computed with an extended LGS, including the aberrations induced by propagation up through the atmosphere and partial correction of the uplink tip/tilt jitter by the LGS pointing loop. The Strehl ratio does not improve at first because the AO control loop was not closed until cycle 11 to give the LGS pointing loop adequate time to converge. The mean Strehl ratio for cycles 21–100 is 0.803, actually slightly higher than achieved with a point source LGS. From this result, we conclude that (i) the static gain and bias calibration formulas for extended laser guide stars have been implemented properly, and (ii) an extended LGS compensates for some fraction of speckle noise by smoothing the subaperture guide star images, at least in the case of zero measurement noise.

6.3 Misregistration

Figure 3 plots Strehl ratio time histories in K band for a conventional NGS AO system of order 8 by 8 with several different values for DM misregistration. These results are once again for an 8 meter telescope aperture diameter and median Cerro Pachon seeing conditions. System performance is not appreciably degraded by a DM misregistration of 0.2 subapertures, perhaps because the direction of misregistration was chosen parallel to the wind velocity and might therefore compensate in part for the effect of servo lag. System performance is significantly degraded by a

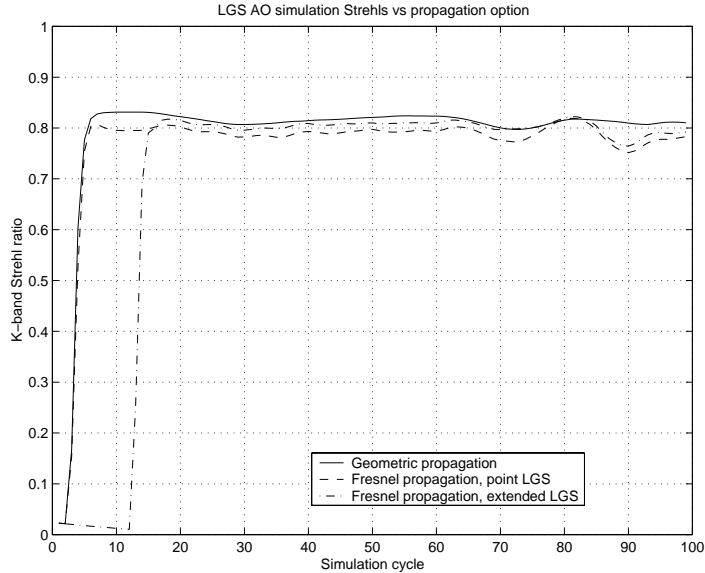


Figure 2: Impact of Diffraction Effects on LGS AO Simulation Results

These Strehl ratio time histories are for the median Cerro Pachon turbulence profile, an 8 meter telescope aperture diameter, a conventional LGS AO system of order 16 by 16, on-axis NGS and LGS, and an 800 Hz update rate. See the text and Table 6 in Section 7 for further details.

DM misregistration of 0.4 subapertures, and a misregistration of 0.6 subapertures causes the control loop to become unstable. These results are not inconsistent with other studies that have shown greater sensitivity to misregistration for standard least squares wavefront reconstruction, since the minimal variance reconstructor used in this simulation filtered out 8 of the highest spatial frequency modes (out of 60 total modes) that are presumably the most sensitive to misregistration.

7 RESULTS FOR GEMINI SOUTH MCAO

In this section, we present a range of sample simulation results generated in support of the Preliminary Design Review for the Gemini-South MCAO system. The principal goal of these studies is to understand how MCAO performance is influenced by higher-order effects such as diffraction, DM misregistration, and imperfect calibration for non-common path errors.

7.1 Parameter Summary

All of the simulation results described in this section are based upon a 7-layer discrete fit to the median Cerro Pachon atmospheric turbulence profile. The altitudes, relative strengths, and windspeeds for the 7 layers are listed in Table 5. Please note that we have slightly (and inadvertently) increased the value of r_0 from 0.155 meters to 0.166 meters for this turbulence profile, thereby reducing the mean-square wavefront error by a factor of $(0.155/0.166)^{5/3} = 0.892$. Exponentiating all of the Strehl ratios presented below to the power of $1/0.892=1.12$ (i.e., $0.8^{1.12} = 0.779$) should compensate for this error with reasonable accuracy. The isoplanatic angle for this profile is approximately 2.75 arc

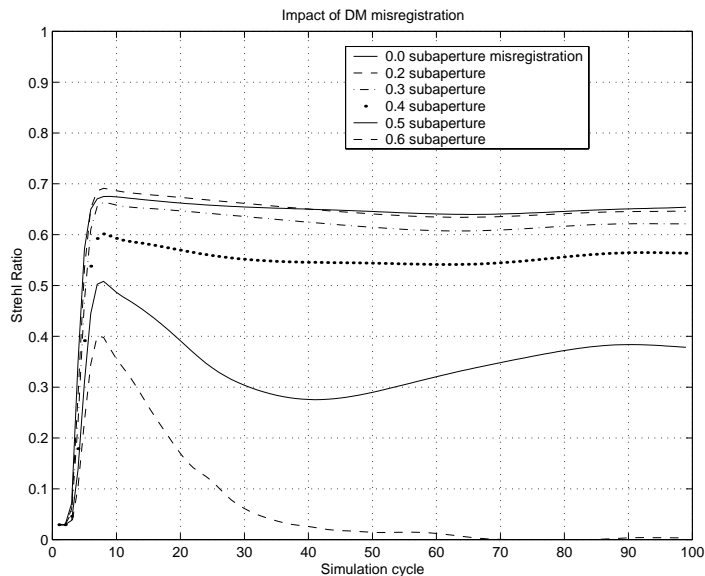


Figure 3: Impact of DM Misregistration

These Strehl ratio time histories are for the median Cerro Pachon turbulence profile, an 8 meter telescope aperture diameter, a conventional NGS AO system of order 8 by 8, an on-axis NGS, and an 800 Hz update rate. See the text and Table 6 in Section 7 for further details.

seconds.

Table 6 lists the basic AO system parameters used for the all of the following simulations unless otherwise specified. These values are generally in close agreement with the parameters for the Gemini-South MCAO design except as noted in the table caption.

One feature of the wavefront reconstruction algorithm used in these simulations that deserves discussion is the treatment of partially illuminated WFS subapertures at the edge of the pupil, as well as edge DM actuators that couple very weakly into the WFS measurements. For simulations using the geometric optics WFS model, the DM-to-WFS influence matrix G is still known accurately for all edge subapertures and actuators, and all of these elements can be used for wave front control using the standard formula for the minimal variance wave front reconstructor. In simulations (and real world AO system) using wave optics, we have found that it can be very difficult to properly calibrate the WFS measurements from weakly illuminated subapertures on account of (i) the different shape of the Shack-Hartmann spot, and (ii) the differences in the influence matrix coefficients. AO loop performance consequently appears to be more sensitive to misregistration and non-common path wave front errors when measurements from very weakly illuminated WFS subapertures are used for wave front reconstruction. In these simulations, the WFS measurement vector is restricted to measurements from subapertures that are at least 40% illuminated. This increases the number of DM edge actuators that couple into the pupil but are in the null space of G , and we have used a simple nearest-neighbor slaving algorithm for these actuators.

Of course, deleting edge subapertures and actuators in this fashion decreases the order of the AO system and may increase the residual wavefront fitting error. This is not the case for the 40% per cent illumination threshold used here, since analytical Strehl ratio calculations (based upon geometric optics) yield virtually identical Strehl ratios for MCAO whether or not these subapertures are included.

Layer	Altitude, m	Fractional Strength	Windspeed, m/s
1	0	0.6475	5.0
2	2077	0.1111	10.0
3	3414	0.0774	15.0
4	5562	0.0439	20.0
5	7212	0.0245	30.0
6	13091	0.0810	20.0
7	15840	0.0146	10.0

Table 5: Atmospheric Turbulence and Windspeed Profiles

This profile is based upon median seeing conditions at Cerro Pachon. Note that the layer altitudes are expressed in terms of the altitude above the site.

Laser Subsystem Parameters		
Number of LGS	5	
LGS locations in field	(0", 0") and ($\pm 30''$, $\pm 30''$)	
LGS signal level at WFS	125 PDE's s/cm ² /sec	
Transmitted beam quality	Diffraction limited	
Beam 1/e ² diameter	0.3 m	
Launch telescope diameter and location	0.45 m, on-axis	
Sodium layer range	99 km	
Adaptive Optics Module		
Number of DM's	3	
Conjugate ranges	0.0, 4.5, 9.0 km	
Actuator pitch	$D/16$, $D/16$, $D/8$	
Number of WFS	5 (LGS)	4 (NGS)
WFS order	16 by 16	Tip/tilt
WFS pixel subtense on the sky	1.0 arc sec	0.5 arc sec
WFS read noise	6 electrons	0 electrons
WFS sampling rate	800 Hz	
Control System		
Control algorithm	Minimal variance	
Processing latency + read time	1.25 ms	
-3 dB closed loop bandwidth	32 Hz	

Table 6: MCAO System Simulation Parameters

These parameters were used for all of the simulations presented in this section except where otherwise indicated. D is the telescope aperture diameter (8 meters), and PDE is an abbreviation for photodetection events. These parameters correspond to the Gemini-South MCAO system design with the following exceptions: A diffraction-limited laser beam (vs 1.5 xDL), an integrated wavefront reconstruction algorithm for both LGS and NGS WFS measurements, and 4 instead of 3 NGS tip/tilt guide stars. This last modification yields symmetric performance over the 1 arc minute square field of view and simplifies performance evaluation.

Spectral Band	Analysis Strehls			Simulation Strehls		
	Center	Edge	Corner	Center	Edge	Corner
J	0.590	0.478	0.475	0.615	0.509	0.505
H	0.739	0.653	0.649	0.756	0.679	0.674
K	0.843	0.787	0.783	0.854	0.804	0.800

Table 7: MCAO Analysis vs Simulation Strehl Ratios with Geometric Optics

This table plots mean Strehl ratios at the center, edge, and corner of a square 1 arc minute field of view for the atmospheric and AO system parameters summarized in Tables 5 and 6 above.

Finally, all simulations used a propagation grid mesh of 1/32 meter, a grid size of 1680 points, and a total grid width of 52.5 meters unless specified otherwise. Each simulation ran for 100 cycles, with mean Strehl ratios averaged over cycles 11-100.

7.2 Performance Estimates for Geometric Optics

We once again begin with geometric simulations to validate the code against analytic performance predictions. Strehl ratios were evaluated in J, H, and K bands (1.25, 1.65, and 2.2 microns), at the center, edge, and corner of a one square arc minute field of view. The edge and corner values were averaged over all four edges and corners. Table 7 summarizes the results obtained. As usual, the simulation Strehl ratios are slightly higher than the analytical calculations but consistently agree to within 1-3 per cent.

7.3 Diffraction Effects

Like Gaul, the effects of diffraction on MCAO simulation results may be divided into three parts: (i) Diffraction in the Shack-Hartmann wave front sensors; (ii) wave optics propagation effects in the atmospheric and optics; and (iii) wave front sensing with extended laser guide stars. The following three subsections describe simulation results quantifying these effects for the Gemini-South MCAO design.

7.3.1 WFS Gain and Speckle Noise

The tilt measurement gain of a Shack-Hartmann wave front sensor can be viewed as the reciprocal of the width of the guide star image in each subaperture. The width and profile of this image can be estimated using the MTF approach described by Eq.'s (26) and (27) above, but this formula is only an approximation and the precise gain will be somewhat different. This is especially true for the NGS full aperture tip/tilt measurements, since these star images will be partially sharpened via the response of the closed loop AO system. WFS measurements computed from Shack-Hartmann spots will also differ from the ideal geometric measurements (i.e., the average wave front gradient on each subaperture) due to so-called “speckle noise,” which is the error introduced in the quad cell tilt estimate by the residual aberrations in the shape and symmetry of the guide star images. Both of these effects must be understood to obtain satisfactory simulation results.

An AO simulation provides the opportunity to compute both types of WFS measurements simultaneously with the AO loop closed on the geometric measurements, so that the gain and randomness in the wave optics measurements

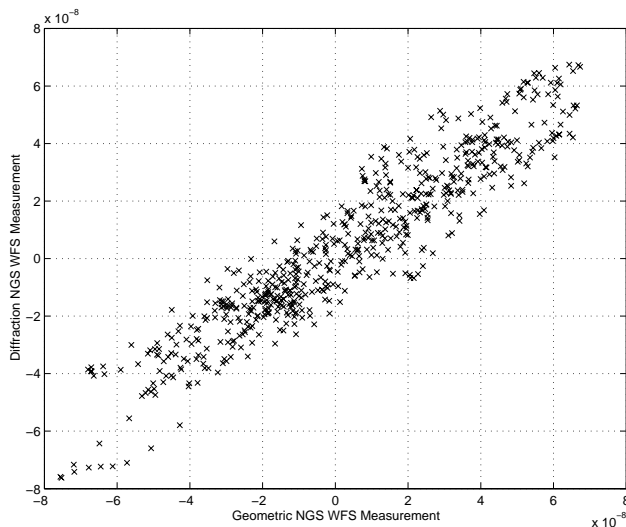


Figure 4: Wave Optics Effects on NGS WFS Measurements

This figure plots NGS tip/tilt measurements computed using a diffraction model for the Shack-Hartmann WFS against the measurements computed for a geometric WFS model (i.e., the average wavefront gradient on the aperture). Both sets of measurements were computed for the same residual wavefront errors with the AO loop closed, and the units are radians of full aperture tilt. The diffraction-based measurements have already been scaled to yield the best linear relationship, and the RMS of the residual scatter is about 0.011 microradians, or 2.3 milli arc seconds.

can be easily quantified via a least squares fit. For the MCAO scenario considered here, the WFS gain estimates computed using an MTF approach are too small by the following factors:

- LGS: 1.15
- NGS: 1.80

These values were computed with diffraction effects modelled in just the WFS, with ideal point source laser guide stars and geometrical propagation through the atmosphere. The value of d/r_0 is about 2.5 for the LGS WFS measurements, so it is not surprising that the long-exposure MTF formula underestimates the WFS gain by a moderate amount. The result for the NGS WFS represents the amount that the PSF has been sharpened by the closed-loop AO system. The improvement is nontrivial but not particularly dramatic, and indicates the limited degree of compensation provided by the AO system at the NGS WFS wavelength of 0.7 microns.

Figure 4 plots the relationship between the closed loop NGS tip/tilt measurements computed using the diffraction and geometric WFS models. The best fit scale factor between the two sets of measurements is unity because the measurements computing by the diffraction model have already been scaled by 1.8^{-1} . Note that the residual NGS WFS measurements errors are very small: The RMS scatter in the fit is only 2.3 milli arc seconds. This is about 0.4 per cent of λ/r_0 , indicating that the large number of speckles in the (very) partially compensated NGS image largely average out. This is a fortunate result, and it would be difficult to obtain with high confidence using any method except for simulation.

The corresponding level of speckle noise for the LGS WFS measurements is about 16.2 milli arc seconds. This is about 2.7 per cent of λ/r_0 at the sensing wavelength, which agrees with the intuition that the size of this error will

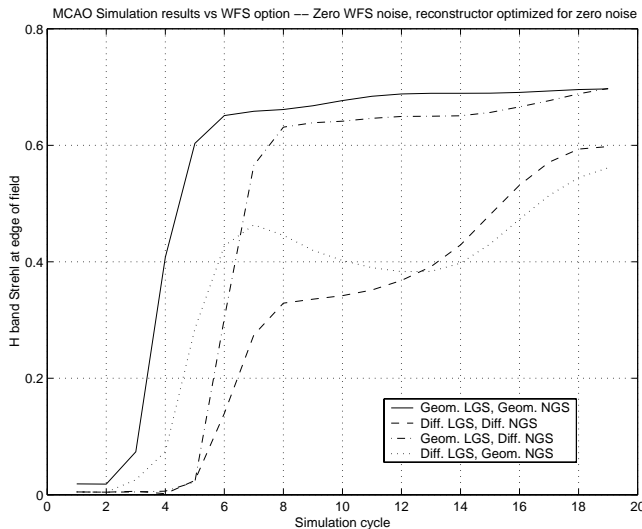


Figure 5: Impact of WFS Diffraction on MCAO Performance for a Reconstructor Tuned for Zero Measurement Noise

This figure plots H band Strehl ratios at one point on the edge of the 1 arc second square field of view for the first few cycles of a MCAO simulation. The reconstruction algorithm has been optimized for noise-free WFS measurements, and is easily confused by the noise-like effects of diffraction in the LGS WFS.

be larger for a few speckles than for many speckles. This small value is still large enough to be a significant source of error for a wave front reconstruction if the control algorithm has been optimized for absolutely zero measurement noise. Figure 5 illustrates Strehl ratio time histories for the first few cycles of a MCAO simulation as a function of the mix of WFS models used, assuming infinite WFS signal levels and a reconstruction matrix optimized for this case. These are H band Strehl ratios at one particular point on the edge of the 1 square arc minute field. The results obtained using geometric models for both the LGS and NGS sensors approach values that are consistent with analytical predictions. Introducing diffraction effects in the NGS WFS has a relatively modest impact on the Strehl ratios achieved, although the Strehls do not begin to increase significantly until the higher-order AO system has started to sharpen the star images in the NGS WFS. The Strehl ratio “tax” for diffraction effects in the LGS WFS is much larger, and remains significant for the entire simulation run. The loss in Strehl is larger than one might expect for WFS measurement noise of only 1/37th of a blur diameter, but the effect is increased because (i) the error is highly correlated from one WFS measurement to the next, and (ii) speaking anthropomorphically, reconstruction algorithms are in a certain sense gullible if they have been designed to expect no WFS measurement noise at all.

Fortunately, this error source can be largely eliminated by using a more realistic (or cynical) reconstruction matrix that has been optimized for a small but non-zero level of WFS measurement noise. The resulting Strehl ratio penalty for using a suboptimal reconstructor corresponds to an RMS optical path difference (OPD) of about 30 nanometers (see Fig. 6), and the additional error induced by speckle noise in the LGS and NGS WFS’s is a much more acceptable 50 nanometers (Fig. 7). This level of error is fairly similar to the results for the conventional LGS WFS presented in Section 6 above, but it does not yet include the effects of wave optics propagation or extended laser guide stars.

7.3.2 Wave Optics Propagation Effects

All of the MCAO simulation results presented to this point are for the case of of ideal point source laser guide stars and geometrical propagation (i.e., ray tracing) through the optics and atmosphere. Fig. 8 illustrates the effect when

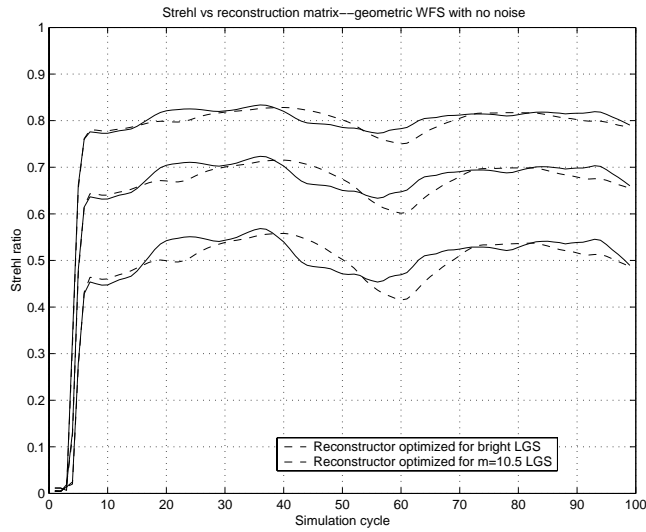


Figure 6: Simulation Results vs. Reconstruction Algorithm for a Geometric WFS Model with Zero Measurement Noise

This figure plots Strehl ratio time histories in J, H, and K bands for one point at the edge of 1 square arc minute MCAO field of view. The two reconstruction algorithms have been optimized for infinite WFS signal levels and zero measurement noise, and for the $m=10.5$ LGS actually specified for Gemini-South MCAO. The WFS measurements are actually noise-free and were computed using the geometric WFS model. The loss of performance for the suboptimal reconstructor corresponds to an RMS OPD of about 30 nanometers.

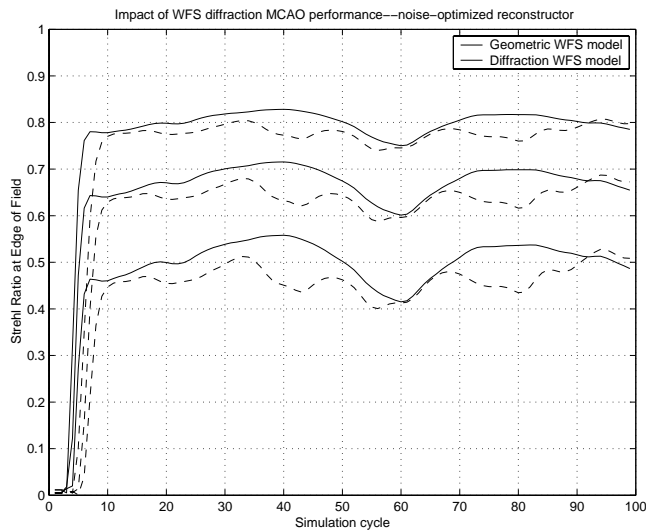


Figure 7: Impact of WFS Diffraction on MCAO Performance for a Reconstructor Tuned for Nonzero Measurement Noise

This figure is similar to Fig. 6 above, except that the two cases plotted correspond to different WFS models (geometric and diffraction) with a common reconstructor optimized for a finite WFS signal level. The Strehl ratios for the diffraction WFS model are smaller by an amount corresponding to a RMS OPD of about 50 nanometers.

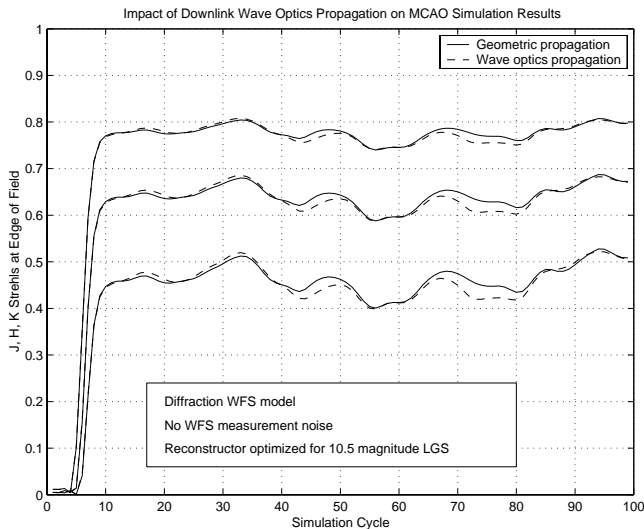


Figure 8: Impact of the Optical Propagation Model on MCAO Simulation Results

This figure is similar to Fig. 6 above, except that the two cases plotted correspond to different optical propagation models (geometrical ray tracing and the near field Fresnel propagator) with a common reconstructor optimized for a finite WFS signal level. The Strehl ratios for the more realistic Fresnel propagator case are smaller by an amount corresponding to a RMS OPD of no more than 22 nanometers.

the nearfield Fresnel propagator is substituted for the geometrical model. The loss in the time-averaged Strehl ratios is very small, corresponding to an RMS OPD of no more than about 22 nanometers in the worst case. The impact of atmospheric scintillation and the suboptimal ordering of the DM's in the Gemini MCAO design can therefore be neglected at IR wavelengths, and appears to be fairly small for visible wavelengths as well.

7.3.3 Extended Laser Guide Stars

The final error source associated with wave optics phenomena is the impact of extended, three-dimensional, laser guide stars. Fig. 9 plots simulated Strehl ratio time histories including this effect. The results obtained for the other propagation options are also plotted for comparison. As for the conventional LGS case presented above in Section 6, the Strehl ratios computed with extended laser guide stars do not begin to increase immediately because the AO loop was not closed until simulation cycle 10. This (probably unnecessary) delay was included to provide the LGS pointing control loops time to converge. Performance after this point is very similar to, and actually slightly superior to, the results with ideal point source laser guide stars. This result is consistent with the conventional LGS AO simulations presented in Section 6 above.

The net effect of diffraction on MCAO simulation results is summarized in table 8. The values are the mean Strehls averaged over cycles 20 through 99 of the simulation. The results presented for the geometrical model are very slightly different from table 7 above, since the results at the edge and corner of the field are for one particular field point instead of averaged over four field points. The overall Strehl ratio losses due to diffraction correspond to RMS OPD's of about 36.3, 53.6, and 63.4 nanometers at the center, edge, and corner of the square 1 arc minute field. The resulting increase in RMS Strehl ratio nonuniformity at three field points, weighted according to Simpson's rule to estimate the loss over the entire field, is about 2.4, 1.4, and 0.8 per cent in the J, H, and K spectral bands. This is our Final Answer for the net effect of diffraction on MCAO performance, at least for this report.

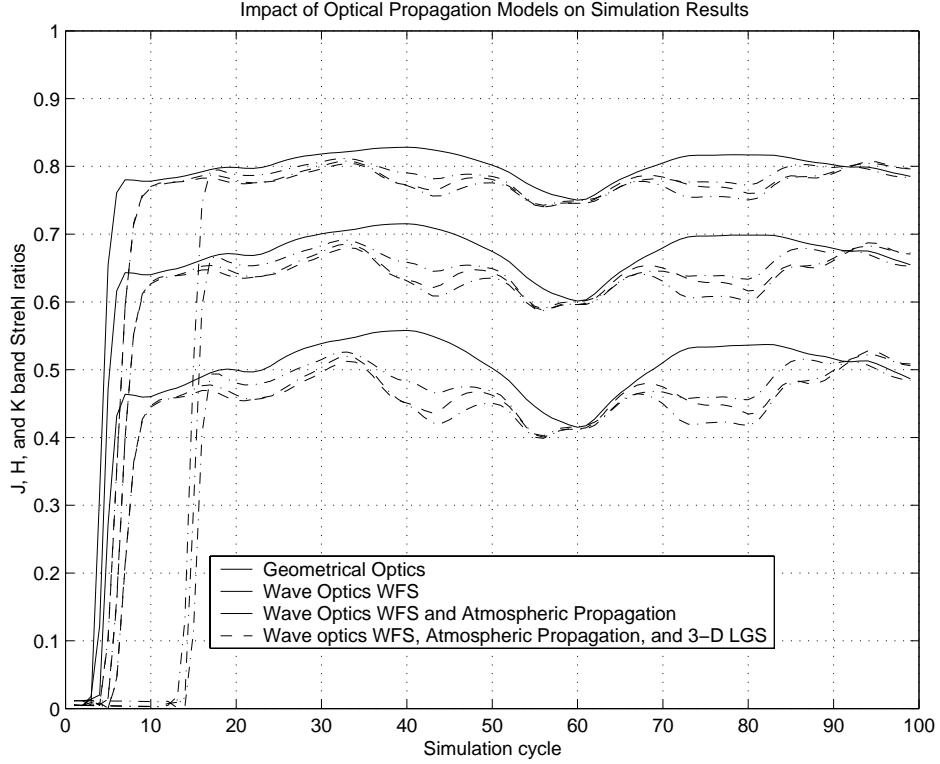


Figure 9: Impact of Optical Propagation Model on MCAO Simulation Results

This figure is similar to Fig. 8 above, except that two additional plots are included for the cases of extended, three-dimensional laser guide stars and idealized geometrical optics. The Strehl ratios computed with extended laser guide stars do not begin to increase immediately because the AO loop was not closed until the tenth simulation cycle.

Spectral Band	Geometric Model			Diffracton Model		
	Center	Edge	Corner	Center	Edge	Corner
J	0.615	0.510	0.493	0.594	0.475	0.446
H	0.756	0.678	0.666	0.742	0.650	0.628
K	0.854	0.803	0.795	0.845	0.784	0.769

Table 8: Overall Impact of Diffraction Effects on MCAO Simulation Results

This table plots time-averaged Strehl ratios at the center, edge, and corner of a square 1 arc minute field of view for the atmospheric and AO system parameters summarized in Tables 5 and 6 above.

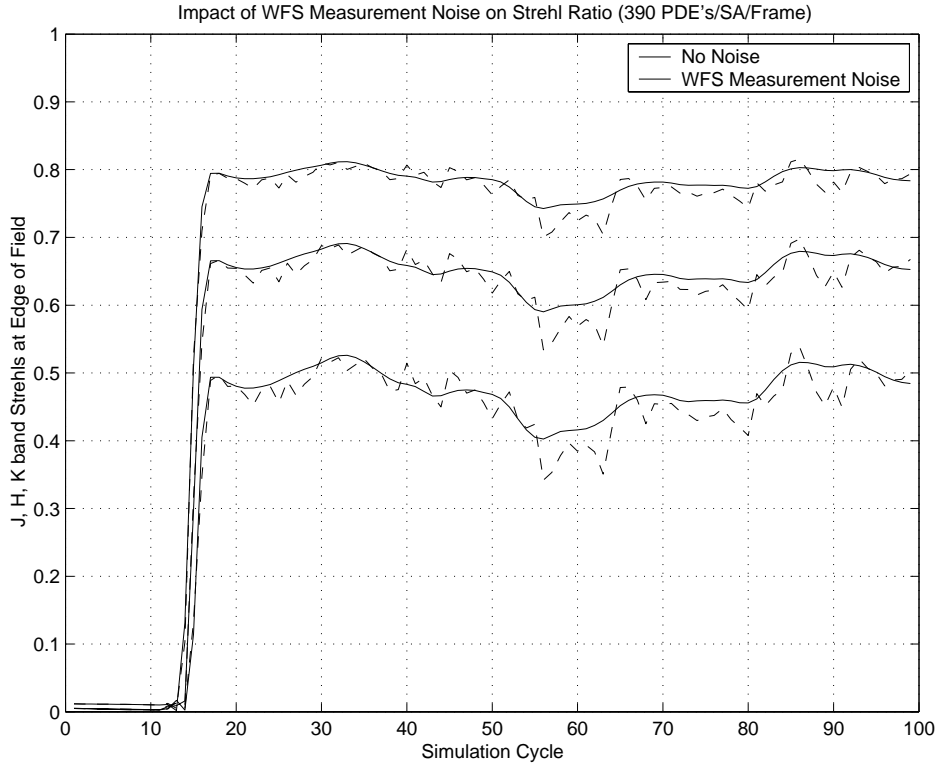


Figure 10: Impact of WFS Measurement Noise on MCAO Simulation Results

These results are similar to Fig. 9, except that they compare MCAO performance with and without LGS WFS measurement noise. Diffraction effects and three-dimensional laser guide stars are modeled, and the reconstruction algorithm has been optimized for the actual LGS WFS noise level as indicated in Table 4. The NGS WFS measurements are still noise free apart from speckle effects.

7.4 WFS Measurement Noise

Figure 10 continues with the present series of results by including the effects of LGS WFS measurement noise. The nominal signal level is 390 photodetection events per frame for a fully illuminated subaperture, and the detector read noise is 6 electrons. The NGS WFS signal level is still infinity. The mean Strehl ratio reduction for cycles 20 through 99 of the simulation correspond to an RMS OPD of about 26.8, 33.6, and 42.3 nanometers at the center, edge, and corner of the 1 arc minute field. The overall Strehl ratio loss due to both noise and diffraction effects together corresponds to RMS OPD's of about 45.1, 63.2, and 76.2 nanometers, which is extremely close to what one would estimate by computing the RSS of the two individual effects. The increase in the RMS Strehl ratio nonuniformity due to both noise and diffraction is about 3.2, 1.9, and 1.0 per cent in the three spectral bands, which is somewhat smaller but similar to what would be obtained by simply summing the two effects. The two effects combine almost linearly (and not in quadrature) because they both depress the Strehl ratio in proportional ways, most significantly at the corners of the field.

The effect of LGS WFS measurement noise on MCAO performance appears to be somewhat smaller in these simulations than was predicted last year at the Conceptual Design Review. There are at least three explanations for this difference:

- The LGS WFS tilt measurement gain in the simulation is about 15-20 per cent greater than the estimate based upon MTF calculations that was used for the CoDR.
- Part of this increase is due to using an ideal Gaussian laser beam in the simulation, however. We believe that the results remain reasonably accurate, because we have still modeled the blurring of the laser guide star by perspective elongation and turbulence on the uplink path. Laser beam quality effects can be included in the simulation as soon as a representative laser beam profile is obtained.
- The CoDR performance summary presented results computed with and without WFS measurement noise for two different reconstruction matrices separately optimized for these different conditions. The reconstruction matrix has been held constant for the current comparison, thereby increasing (as discussed above) the residual wave front errors in the noise free case by about 30 nanometers RMS. This bookkeeping convention reduces the wave front error allocated to LGS WFS measurement noise in the summary MCAO error budgets, but increases the error allocated to anisoplanatism and fitting error by an identical amount.

7.5 DM Misregistration

The final simulation available for the PDR documentation relates to DM misregistration and other sources of calibration error in computing the DM-to-WFS influence matrix. These error include: (i) genuine misregistration between the DM's and the LGS WFS due to flexure and thermal effects, (ii) LGS pointing errors, and (iii) additional misregistration errors induced by the fast tip/tilt mirror, which is not located at a pupil. This last effect is estimated to be considerably smaller than the first two and has not been explicitly included in the simulations.² The PDR estimate for the first error source is a RMS two-axis misregistration of 0.004 times the diameter of the pupil, which we have simulated very generically by placing rotation, magnification, and translation alignment errors of this magnitude on DM9, DM4.5, and DM0. The estimated pointing biases in the LGS locations on the sky are approximately 1 arc second (two-axis, one sigma), and these offsets introduce errors in the DM-to-WFS influence matrix by translating the LGS beamprints on DM9 and DM4.5. We have simulated these biases by picking a single set of normally distributed, zero mean pointing errors. Finally, the dynamic pointing errors due to noise and servo lag in the LGS tip/tilt control loops are already modeled by the simulation.

Fig. 11 illustrates the results obtained with these sample misregistration errors. The reduction in the mean Strehl ratio averaged over cycles 20 to 99 of the simulation corresponds to RMS wave front errors of 25.9, 22.8, and 19.4 nm at the center, edge, and corner of the field.

8 TOWARDS EXTREMELY LARGE TELESCOPES

At first reading, the idea of detailed wave-optics propagation simulations for extremely large telescopes may seem completely impractical. Entry-level proposals for extremely large telescopes such as CELT and GSMT call for roughly a four-fold increase in telescope aperture diameter, implying a 16-fold increase in the number of DM actuators and WFS subapertures even if the number of guide stars, deformable mirrors, and the DM actuator densities are not increased beyond values used for the Gemini-South MCAO design. We are confident that efficient simulations should still be very feasible, however. Significant reductions in the required computer time may actually be possible, assuming that parts of the existing simulation are parallelized and that certain approximations are made in defining the wavefront reconstruction algorithm.

Simulation computations may be broken down very generally into (i) wavefront propagation through the atmosphere and optics, (ii) computing the WFS measurements and applying the DM actuator commands, and (iii)

²It will be intrinsically incorporated when we include a separate fast tip/tilt mirror in the simulation to study windshake and tip/tilt loop dynamics, and place this mirror in the correct conjugate plane.

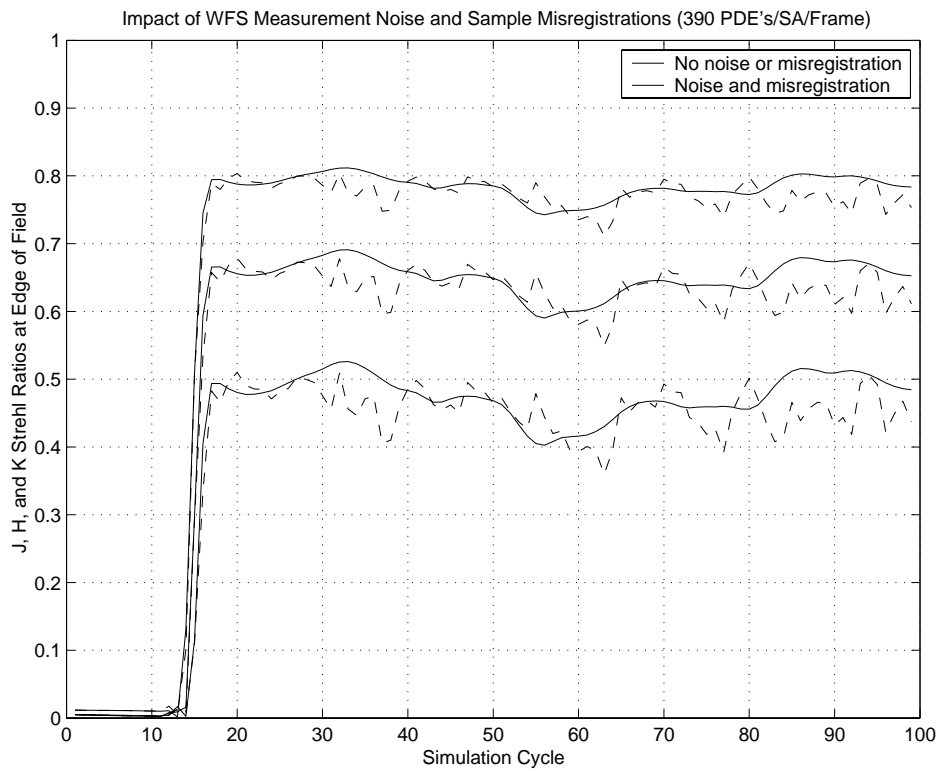


Figure 11: Impact of WFS Measurement Noise and Misregistration Errors

This figure is similar to FIG. 10, except that representative DM-to-WFS misregistration errors and LGS pointing biases have been included in the simulation.

deriving the DM actuator commands from the WFS measurements. The computation requirements for part (i) should not be significantly larger for extremely large telescopes, given that the propagation grid size, the number of DM's, and the number of guide stars do not increase dramatically compared with current simulations for 8-meter telescopes. Recent analytical calculations indicate the number of guide stars and DM's necessary for a given level of MCAO performance is a very weak function of telescope aperture diameter, and that good results for 30 meter telescopes should still be possible with only 5 higher-order guide stars and 3 DM's [5]. The propagation grid size for simulations of thirty meter telescopes need not be much greater than 60 meters, provided only that we can assume a turbulence outer scale of about 30 meters. This is only slightly larger than the 50 meter phase screens we are already using for simulations of Gemini-South MCAO. The length of wall clock time required for wavefront propagations could actually be dramatically reduced via parallel computing, since two-dimensional FFT's are easily parallelized. The necessary routines are already available in standard FFT software packages and can be called from MATLAB.

The computation time required to compute WFS measurements and implement DM actuator commands will scale roughly with the total number of WFS subapertures and DM actuators, particularly if the DM actuator pitch is held constant. But these operations represent only a very small fraction of the total calculations for 8 meter simulations, and this would still be true if the number of subapertures and actuators was multiplied by 16.

This is not the case for simulating the wavefront reconstruction algorithm, however. If implemented as an ordinary matrix multiply, the number of computations per wavefront reconstruction scales with the product of the number of DM actuators and WFS subapertures. Scaling the number of actuators and subapertures by a factor of 16 would yield a factor of 256 increase in computation time (and a similar increase in memory), increasing the time spent on this aspect of the simulation from a small fraction of the time required for the wavefront propagations to the largest single contributor. Even worse, the time spent to compute the minimal variance reconstruction algorithm using current methods will scale with the *cube* of the number of WFS subapertures. Much more efficient approaches to wavefront reconstruction that still provide satisfactory performance will need to be developed to efficiently simulate MCAO on extremely large telescopes.

The standard least squares reconstruction algorithm may be implemented very efficiently using sparse matrix methods because the DM-to-WFS influence matrix G is sparse. In the notation of Section 4.6, this reconstructor is defined by the equation

$$\vec{e} = (G^T G)^{-1} G^T \vec{s}. \quad (33)$$

If G is sparse the intermediate quantity $\vec{f} = G^T \vec{s}$ can be computed efficiently, and then the system $(G^T G)\vec{e} = \vec{f}$ can be solved efficiently for \vec{e} by finding an upper/lower triangular factorization for $(G^T G)$ that is also sparse³. Unfortunately, simulations to date indicate that this reconstruction approach performs poorly without SVD (singular value decomposition) filtering of poorly sensed modes, and the SVD decomposition of a sparse matrix is not necessarily sparse. It has been suggested that “softer” filtering of the poorly sensed modes using the algorithm

$$\vec{e} = (G^T G + \lambda I)^{-1} G^T \vec{s}, \quad (34)$$

should be considered, since the matrix $(G^T G + \lambda I)$ is no less sparse than $(G^T G)$. More generally, any system of the form $(G^T G + S + L)\vec{e} = \vec{f}$, where S is sparse and L is low rank, can be solved efficiently and could be considered as part of a candidate reconstruction algorithm. These approaches could be first evaluated and optimized in 8-meter simulations, where the the optimized minimal variance estimation algorithm is practical to run and can be used as a performance benchmark.

Acknowledgements

This reserach was supported by the Gemini Observatory, which is operated by the Association of Universities for Research in Astronomy, Inc., under a cooperative agreement with the NSF on behalf of the Gemini Partnership:

³This can be accomplished by permuting the order of the DM actuators

the National Science Foundation (United States), the Particle Physics and Astronomy Research Council (United Kingdom), the National Research Council (Canada), CONICYT (Chile), the Australian Research Council (Australia), CNPq (Brazil), and CONICET (Argentina).

REFERENCES

- [1] J.M. Beckers, “Detailed Compensation of Atmospheric Seeing using Multi-Conjugate Adaptive Optics,” *SPIE* **1114**, 215–217 (1989).
- [2] D.C. Johnston and B.M. Welsh, “Analysis of multiconjugate adaptive optics,” *J. Opt. Soc. Am. A* **11**, 394–408 (1994).
- [3] B.L. Ellerbroek, “First-order performance evaluation of adaptive-optics systems for atmospheric-turbulence compensation in extended-field-of-view astronomical telescopes,” *J. Opt. Soc. Am. A* **11**, 783–805 (1994).
- [4] T. Fusco, J.-M. Conan, V. Michau, L.M. Mugnier, and G. Rousset, “Phase estimation for large field of view: application to multiconjugate adaptive optics,” *SPIE* **3763**, 125–133 (1999).
- [5] B.L. Ellerbroek, “Scaling Multi-Conjugate Adaptive Optics Performance Estimates to Extremely Large Telescopes,” *SPIE* **4007**, 1088-1099 (2000).
- [6] E.P. Walner, “Optimal wave-front correction using slope measurements,” *J. Opt. Soc. Am.* **73**, 1771–1776 (1983).
- [7] B.M. Welsh and C.S. Gardner, “Effects of turbulence-induced anisoplanatism on the imaging performance of adaptive-astronomical telescopes using laser guide stars,” *J. Opt. Soc. Am. A* **8**, 69–80 (1991).
- [8] G.A. Tyler, “Merging: a new method for tomography through random media,” *J. Opt. Soc. Am. A* **11**, 409–424 (1994).
- [9] R. Flicker, B.L. Ellerbroek, and F.J. Rigaut, “Comparison of multiconjugate adaptive optics configurations and control algorithms for the Gemini-South 8m telescope,” this volume.
- [10] J. Vernin, A. Agabi, R. Avila, M. Azouit, R. Conan, F. Martin, E.Masciadri, L. Sanchez, and A. Ziad, *1998 Gemini Site Testing Campaign: Cerro Pachon and Cerro Tololo*, (Gemini Project, 2000).
- [11] J. W. Goodman, *Introduction to Fourier Optics*, McGraw-Hill, New York, 1968.